Geophysical Research Letters

RESEARCH LETTER
10.1029/2022GL101412

Diurnal Sea Surface Temperature Warming Along the Kuroshio off Taiwan Under Easterly Wind Conditions

Ming-Huei Chang[1,2], Yu-Hsin Cheng[3], Yu-Yu Yeh[1], Je-Yuan Hsu[1], Sen Jan[1], Yu-heng Tseng[1,2], Chung-Hsiung Sui[4], Yiing Jang Yang[1,2], and Po-Hsiung Lin[4]

[1]Institute of Oceanography, National Taiwan University, Taipei, Taiwan, [2]Ocean Center, National Taiwan University, Taipei, Taiwan, [3]Department of Marine Environmental Informatics, National Taiwan Ocean University, Keelung, Taiwan, [4]Department of Atmospheric Sciences, National Taiwan University, Taipei, Taiwan

Key Points:

- Lagrangian observations and satellite remote sensing reveal inhomogeneous diurnal surface temperature warming along the Kuroshio path
- Inhomogeneous diurnal surface warming is due to terrain-induced bifurcated wind and the strong Kuroshio flow speed
- The critical wind speed of ~2 m s^{-1} relative to the current determines whether the solar heat could transfer deeper via shear instability

Supporting Information:

Supporting Information may be found in the online version of this article.

Correspondence to:

M.-H. Chang,
minghueichang@ntu.edu.tw

Citation:

Chang, M.-H., Cheng, Y.-H., Yeh, Y.-Y., Hsu, J.-Y., Jan, S., Tseng, Y.-h., et al. (2023). Diurnal sea surface temperature warming along the Kuroshio off Taiwan under easterly wind conditions. *Geophysical Research Letters*, *50*, e2022GL101412. https://doi.org/10.1029/2022GL101412

Received 23 SEP 2022
Accepted 11 JAN 2023

Abstract We carry out the Lagrangian diurnal warm layer (DWL) observations, supplemented by satellite products, along the strong Kuroshio east of Taiwan, where the boundary terrain modifies the winds and the advection effect is significant. The synoptic easterly wind bifurcates as it encounters Taiwan's coast, forming the southward-blowing and the northward-blowing branches in the southern and northern regions of the bifurcation, respectively. The two branches produce areas with enhanced and weakened apparent wind speed relative to the northeastward flowing Kuroshio. The DWL can reach 5 m in the south of the bifurcation due to the shear instability-induced mixing. Sea surface temperature (SST) enhancement occurs around and in the north of the wind bifurcation, where the solar heat is only trapped in the upper 2 m due to the absence of instability, forming inhomogeneous SST along the Kuroshio. The synoptic wind variations and Kuroshio advection further modulate the location of SST enhancement.

Plain Language Summary Sea surface temperature could change in a day due to solar heating over the top few meters, where a thin surface warm layer is created. This layer's thickness and mean temperature are related to solar heating and wind speed. The wind blowing works like a stick stirring the surface water to spread the surface heat from the sun to the deeper ocean and, therefore, affect the thickness of the upper ocean's warm layer. However, the warm layer and its associated surface temperature variation exist only in the weak to moderate wind (0–4 m s^{-1}). In the region of a strong current, such as the western boundary current, the moving speed of surface water (1–2 m s^{-1}) is comparable to the wind speed suitable for warm layer formation. It is essential to use the wind speed that the surface waters "feel" as they move to evaluate the warm layer. We found that the above effect has resulted in the asymmetric sea surface warming along the Kuroshio in response to the daily solar heating.

1. Introduction

Sea surface temperature (SST) is important in linking the global ocean-atmosphere system due to its critical role in the latent, sensible, and radiative heat fluxes between the atmosphere and ocean (Fairall et al., 2003). The importance of SST in accurately forecasting both severe typhoon events and daily weather (Emanuel & Sobel, 2013; Wu et al., 2007) and tropical intraseasonal oscillations (Sui et al., 1998) has been recognized. SST could change daily in response to the absorption of solar radiation over the top few meters, where a thin diurnal warm layer (DWL) is created. The thickness and mean temperature of this layer are predominantly controlled by (a) net surface heating, (b) wind speed (Kawai & Wada, 2007; Price et al., 1986), (c) subsurface ocean mixing associated with the small-scale to submesoscale oceanic processes (e.g., D'Asaro et al., 2011), and (d) the current advection effect on the near-surface water (Shcherbina et al., 2019). Understanding the processes in the formation and evolution of DWL is essential for predicting SST (Masich et al., 2021; Thompson et al., 2019). Typically, daytime increases in temperature on the near-surface cause stratification in the upper 10 m. The stratified layer is a slippery interface where the turbulent mixing is suppressed. As a result, surface fluxes of momentum and heat are trapped in the DWL above the slippery interface, forming a warm diurnal jet flowing typically at 0.1–0.3 m s^{-1} (Hughes et al., 2020; Price et al., 1986; Sutherland et al., 2016; Wijesekera et al., 2020). Diffusion of heat occurs slowly during the daytime due to the presence of DWL, but then rapidly upon the onset of nighttime cooling and convectively driven mixing due to surface heat loss by longwave radiation and latent heat flux.

The SST around the land boundary could significantly vary in space, different from that in the open ocean. For instance, a region of enhanced SST was observed in the wind-sheltered area south of Gran Canaria (Basterretxea et al., 2002; Caldeira & Marchesiello, 2002). The warm region formed because the daytime solar radiation heats and stabilizes the surface layer under weak wind conditions. In contrast, the wind-induced mixing outside the lee reduces SST. Inherently, the low wind region occurs not only on the downwind side of an orographic obstacle but also on the windward side, where the wind could weaken due to the blocking effect. It occurs particularly when the coastline of steep terrain facing the wind is sufficiently long.

SST enhancement on the windward side could be a ubiquitous nearshore process since the world sea is bounded by coastal lines where the cross-shore synoptic wind and sea-land breeze could prevail. In addition, the coastal ocean often has an alongshore current flowing at speed comparable to the wind speed required for developing DWL. Taiwan is a mountainous island in the northwestern Pacific Ocean (Figures 1a and 1b). The terrain along eastern Taiwan rises abruptly to more than 1,500 m in height within 20–30 km from the shoreline (Yu & Lin, 2017). The terrain often modifies the synoptic-scale wind field. For example, a convective band of cloud and precipitation commonly occurs at 30–50 km off the coastline due to the encountering of a weak landward (easterly) synoptic-scale wind and offshore wind (Alpers et al., 2007; Yu and Lin, 2008, 2017). Finally, the Kuroshio flows alongshore and northeastward (Figure 1c) at speeds ranging from 1 to 1.5 m s^{-1}. It will be interesting to explore whether a strong western boundary current can affect the formation of a DWL. This paper presents diurnal SST variations and their physical mechanisms along the Kuroshio off Taiwan by analyzing the data taken by an along-stream drifting metocean buoy, geostationary satellite SST, and blended wind product.

2. Field Observations and Satellite Data

On 5–10 September 2021, we performed the research cruise onboard the *R/V New Ocean Researcher 2*. A 45" spherical buoy equipped with meteorological (Figure 1d) and oceanic sensors (Figure 1e) above the sea surface and under the water, respectively, was deployed off southeast of Taiwan, which in turn drifted northeastward along the Kuroshio (black line in Figure 1c) to measure the metocean variations. The meteorological sensors included a propeller anemometer mounted at 2.2 m height, a radiometer, and an all-in-one instrument (Figure 1d). The 10-m wind speed, obtained by using the logarithmic extrapolation of the wind speed observed at 2.2 m height, was used for the following analysis. We defined the wind direction as the direction the wind blew to, consistent with the current direction. A 1,200-kHz acoustic Doppler current meter (ADCP) was mounted on the buoy and looked downward (Figure 1e). Fifty-two temperature sensors were distributed in a 20-m chain tethered by the buoy (the vertical resolution is 0.3–1 m, as shown by the black dots in Figure 3b). The sampling interval of ADCP and temperature sensors was 10 s (see Text S1 in Supporting Information S1 for details of data processing). The vertical resolution is 1 m (black dots in Figures 3c and 3d). The metocean buoy freely drifted 245 km for 46 hr along the Kuroshio and recorded two diurnal warming events.

Sixteen newly developed radiosondes (Hwang et al., 2020; Figure 1c) were launched during our cruise to record the vertical wind profile. The hourly mereological data at Hualien station (star signs in Figure 1), maintained by Taiwan's Central Weather Bureau, were used to supplement our analysis. Satellite products were introduced in Text S2 in Supporting Information S1. The local time (UTC + 8:00) was used throughout this paper.

3. Results

3.1. Surface Warming Along the Kuroshio

During our experiment, the easterly synoptic wind (~5 m s^{-1}) bifurcated as it encountered Taiwan's coast, forming the southward-blowing and the northward-blowing winds in the southern and northern regions of the Kuroshio off Taiwan, respectively, both of which have a speed of 1–4 m s^{-1} (Figures 1a and 1b). We also demonstrated the terrain effect on the winds using the trajectories of radiosondes (Figure 1c). The translating directions of the upstream and downstream Kuroshio radiosondes were respectively southwestward and northwestward in height lower than Taiwan's mountains (~3,500 m; light blue—deep blue color scale in Figure 1c), in agreement with the nearshore bifurcation wind pattern. Higher than ~3,500 m, the wind directions became primarily westward, coinciding with the synoptic wind in the far field. SST enhancements in the daytime were found on the downwind side off the southwest of Taiwan and the windward side, where the wind bifurcated (Figure 1a), but were absent in the nighttime (Figure 1b). The SST warming on the downwind side resembles that reported in Basterretxea

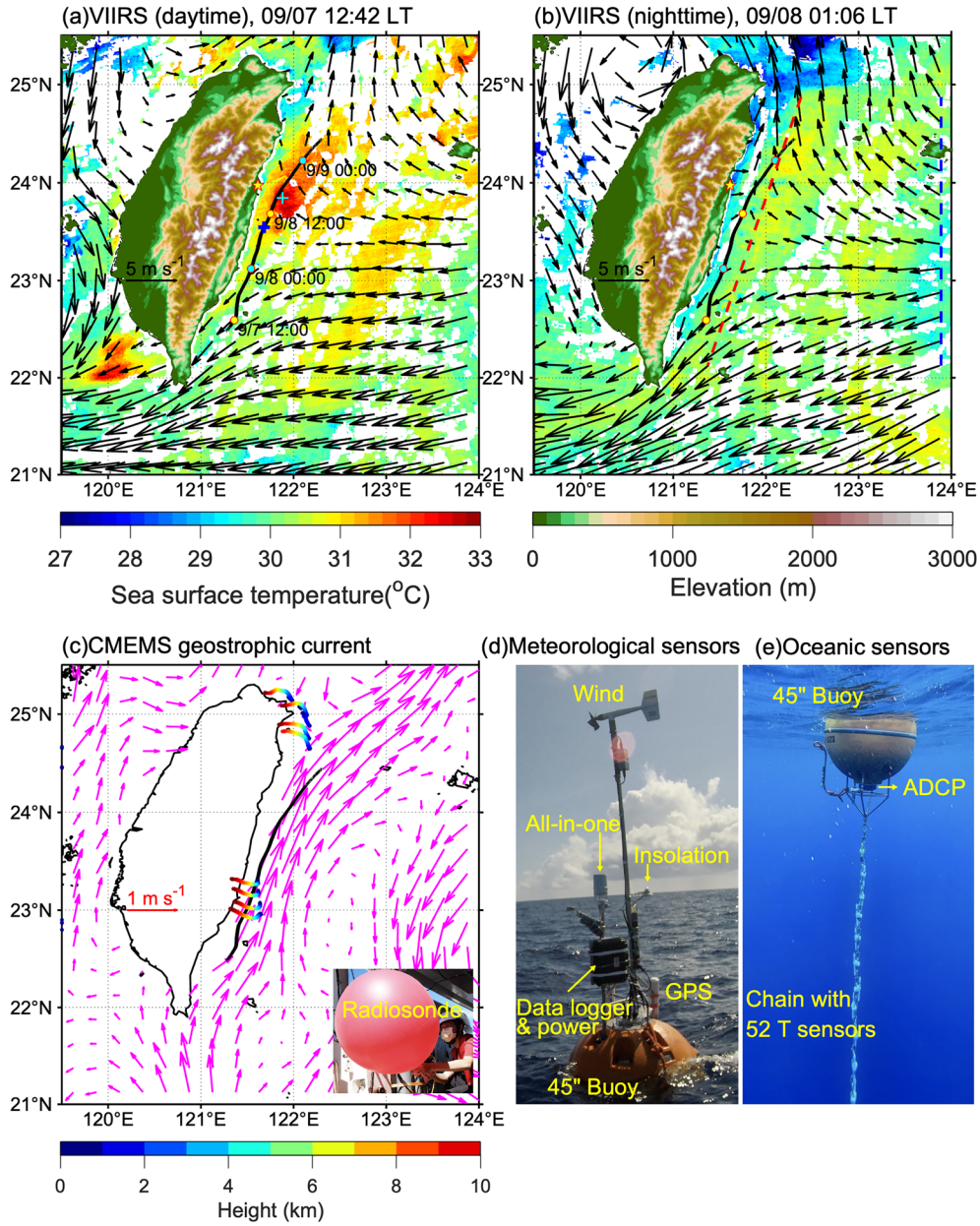

Figure 1. The terrain of Taiwan and sea surface temperature (SST) in the (a) daytime (12:42, 7 September) and (b) nighttime (01:06, 8 September), respectively, obtained from VIIRS. The wind vectors (blowing toward) obtained from CCMP in panels (a and b) are at 08:00, 7 September and 02:00, 8 September, respectively. (c) Current vectors around Taiwan derived from CMEMS satellite altimetry on 7 September and trajectories of radiosondes colored by height. (d) Atmospheric and (e) oceanic instruments equipped with the 45" metocean buoy. The black curves in panels (a–c) are the drifting track of the buoy. The star signs in panels (a and b) denote the location of Hualien station. The blue and cyan plus signs in panel (a) indicate the wind bifurcation point at 08:00 on 7 September and the center of warm water with SST >32°C, respectively. The red dashed line in panel (b) is the along-Kuroshio transect used to examine the SST variations in 2021, shown in Figure S1 in Supporting Information S1. The blue dashed line in panel (b) is the transect, where the wind vectors are averaged to represent the synoptic wind vector, as shown in Figures S1a and S1b in Supporting Information S1.

et al. (2002) and Caldeira and Marchesiello (2002). Our particular interest is the SST warming on the windward side, which has received far less attention.

Our metocean buoy freely drifted 245 km along the Kuroshio (black curve in Figure 1c) and across the region of wind bifurcation and SST enhancement (black curve in Figure 1a) at a mean speed of ~1.5 m s^{-1}. We linearly interpolated the AHI SST value on the buoy track for comparison. Time-distance plot (0 and 245 km at the

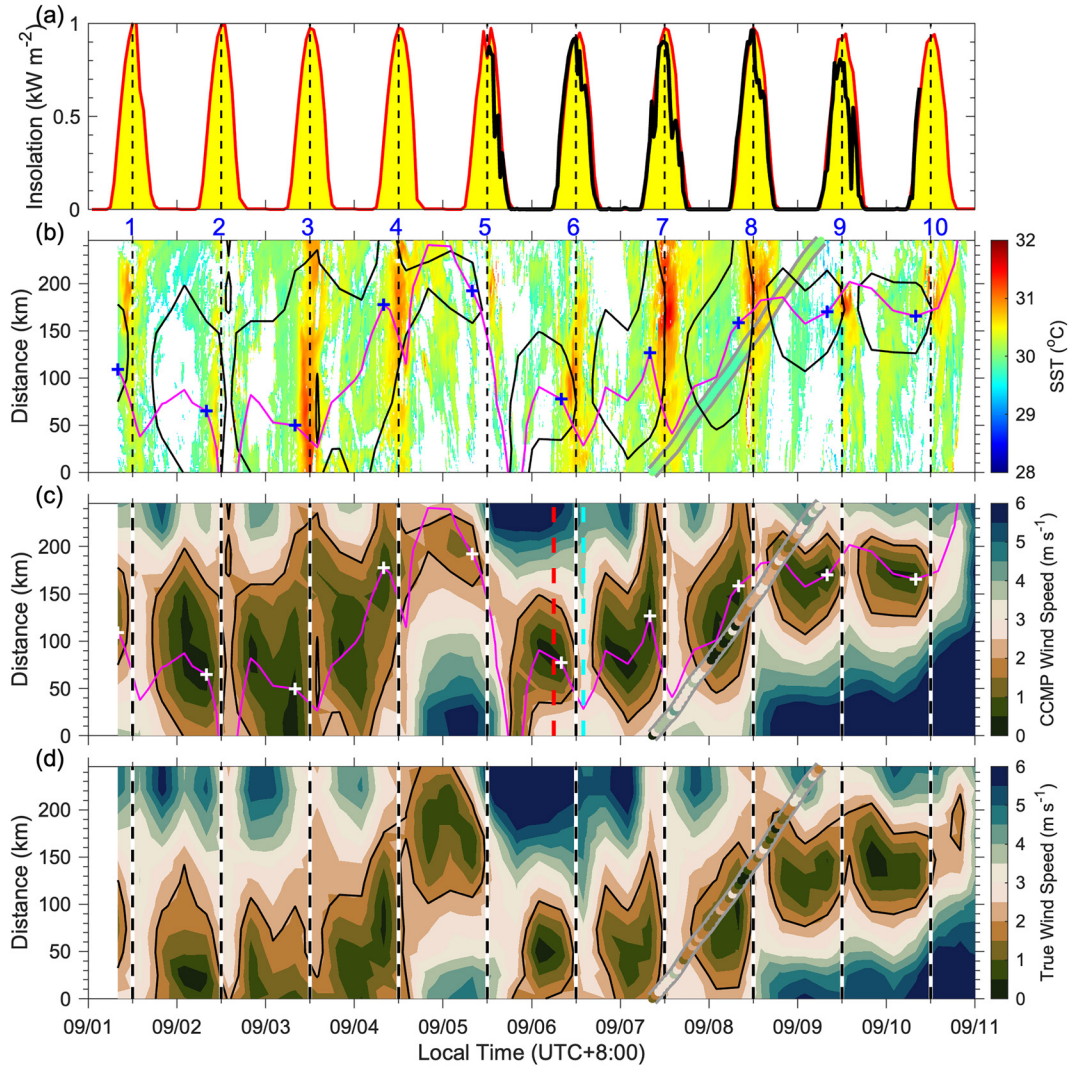

Figure 2. (a) Time series of insolation measured from Central Weather Bureau Hualien station (red curve; 1–10 September) and onboard the *R/V NOR2* (black curve; 5–10 September). Time-distance (along the buoy track) contours of panel (b) AHI sea surface temperature (SST), (c) CCMP apparent wind speed, and (d) CCMP true wind speed. Colored bands enclosed by the gray line in panel (b–d) are the SST, apparent wind speed, and true wind speed, respectively, observed by the buoy. Black vertical dashed lines denote the time at noon. The red and cyan dashed lines in panel (c) indicate the typical time when the land breeze (06:00) and the sea breeze (14:00) have a maximum. The black contour lines in panels (b–d) are the 2 m s^{-1} isotach. The magenta lines in panels (b and c) are the 0 m s^{-1} isotach of meridional wind. The blue plus signs in panel (b) and the white plus signs in panel (c) indicate the wind bifurcation points at 08:00.

southmost and northmost of the buoy track, respectively) of AHI SST on 1–10 September (Figure 2b) showed 10 events of SST increase (numbered 1–10) that correspond to the daily insolation (Figure 2a). The insolation at Hualien (red line in Figure 2a) mostly agreed with that observed in our *R/V* (black line Figure 2a) and had a maximum of ~1 kW m^{-2} at noon. The diurnal SST increase was about 1–3 hr lag from the insolation maximum but revealed a significant meridional (along-track) difference. Event 2 was unclear due to the cloud-induced insufficient data. Mostly, the SST increase was remarkable in the north portion of the track (warming events 1, 5, 7, 8, 9, and 10). Warming events 3 and 4 showed a relatively homogeneous SST increase along the track. Warming event 6 showed an enhancement in the south of the buoy track. The SST measured using our metocean buoy (Figure 2b) agreed with the AHI SST. We deployed the metocean buoy at 8:40 a.m. on 7 September and recovered it at 6:20 a.m. on 9 September. The buoy experienced a weaker SST increase (30.3°C) in the upstream Kuroshio on 7 September and a significant SST increase (30.8°C) in the downstream Kuroshio on the next day (colored band enclosed by the gray line in Figure 2b). Similarly, the CCMP wind speeds were examined as follows.

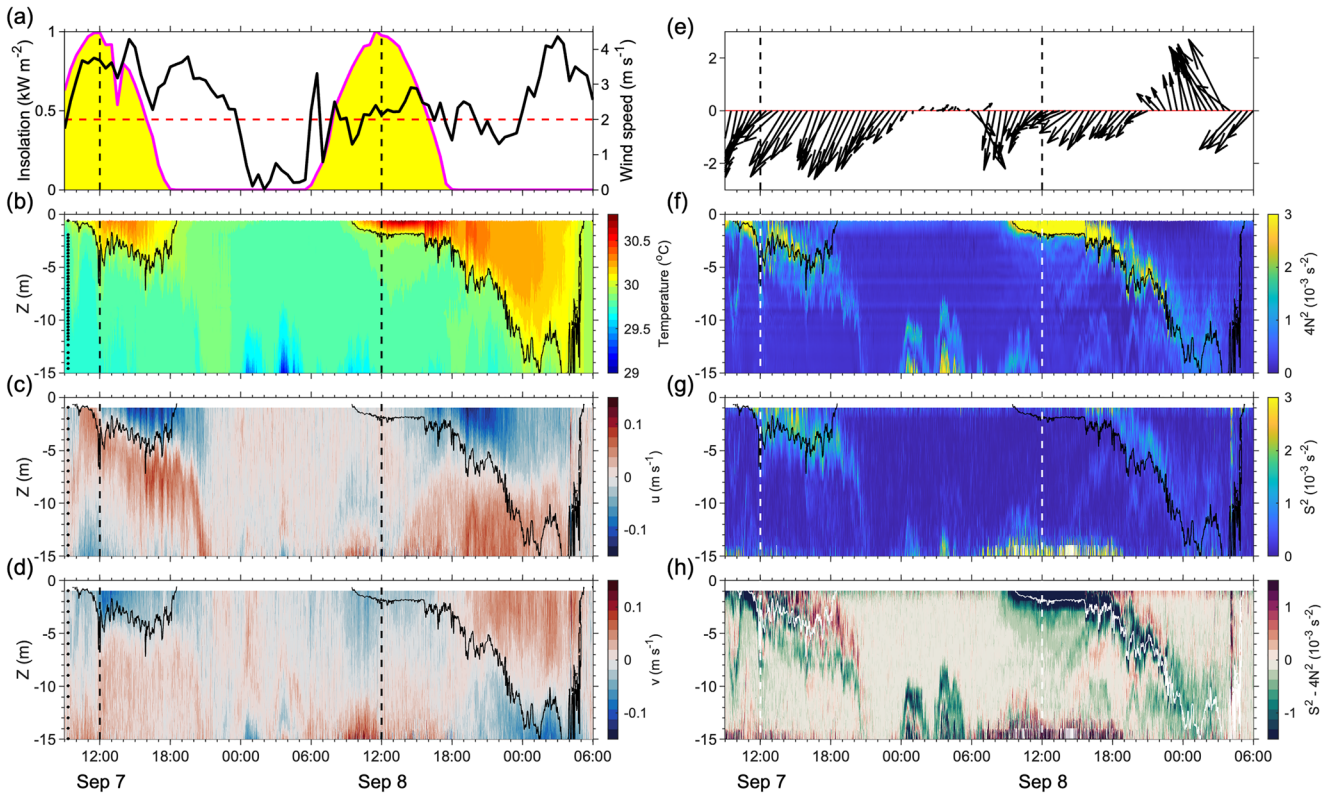

Figure 3. (a) Time series of insolation (magenta line) and apparent wind speed (black line). Contour plots of (b) temperature, (c) zonal velocity, and (d) meridional velocity. (e) Apparent wind vectors as a function of time. Contour plots of (f) $4N^2$, (g) S^2, and (h) S^2–$4N^2$. The vertical dashed lines denote the time at noon. The horizontal red dashed line in panel (a) indicates the wind speed of 2 m s^{-1}. The black contour lines in (b–d, f, and g) are the 30°C isotherm. The white contour line in panel (h) is the 30°C isotherm. The black dots in panel (b) show the locations of temperature sensors. The black dots in panels (c and d) show the measuring depths of acoustic Doppler current meter velocity.

The CCMP product is microwave-derived apparent winds relative to the moving ocean surface (Atlas et al., 2011; Mears et al., 2019). The predominant feature, as revealed in the similar time-distance plot (Figure 2c) via linear interpolation, was the 100–200 km width low wind (<2 m s^{-1}) region that meridionally migrated. The low wind region characterized the area of easterly wind bifurcation captured in Figures 1a and 1b. The daily variations of SST were modulated by the sea-land breeze circulation (Chen et al., 1999, see Text S3 in Supporting Information S1). Our measured apparent (current-following) wind speeds agree with the CCMP winds well (colored band enclosed by the gray line in Figure 2c). The spatial variation of significant SST warming can be captured in the region where wind speed is <2 m s^{-1}. In the daytime, the low wind region having wind speeds <2 m s^{-1} was collocated with the enhanced SST (30.5°C–32°C). Outside the low wind region, the SST is 29°C–30.5°C under moderate wind conditions (2–6 m s^{-1}). The true wind velocity was obtained by taking the vector sum of the apparent wind velocity and current velocity derived from the drifting velocity of the buoy. The time-distance plot of true wind speed (Figure 2d) showed a southward shift of the low wind region. This well reflects that the southward and northward blowing wind strengthens and weakens, respectively, in the frame of northeastward flowing currents. As a result, the bifurcating region characterized by the apparent wind speed migrates northward. The SST variations were related to the apparent wind speed where the Kuroshio current was accounted for instead of the true wind speed.

We further clarify the relationship between the bifurcation point and the SST warming. The bifurcation center is defined as the point along the buoy trajectory where the meridional wind velocity is 0 m s^{-1} (magenta lines in Figures 2b and 2c). The bifurcation center at 08:00, when the wind should be most effective for the SST variations, is chosen to compare with the along-track SST variations (plus signs in Figures 2b and 2c). The slight meridional variations of the synoptic wind direction lead to the change of the bifurcation center in 50–200 km. It is found that the strong SST enhancement mainly occurs around and in the north of the wind bifurcation region (Figure 2c). The VIIRS SST shown in Figure 1a lends further support.

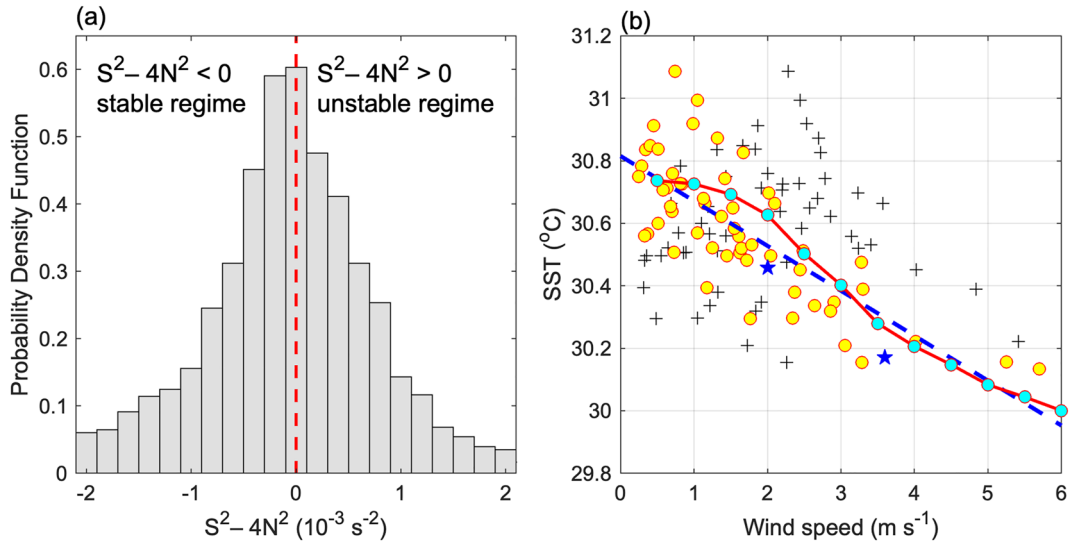

Figure 4. Probability density function of reduced shear squared S^2–$4N^2$ represented as a histogram plot. (b) Scatter plots between CCMP apparent wind speed and AHI sea surface temperature (SST) (yellow dots), between CCMP true wind speed and AHI SST (plus signs), and between measured apparent wind speed and measured SST (blue stars). The red dashed line in panel (a) denotes S^2–$4N^2 = 0$. The blue dashed line in panel (b) represents the linear regression fit to the CCMP apparent wind speed and AHI SST. The cyan dots connected by the red line in panel (b) are the Price-Weller-Pinkel (Price et al., 1986) results given the wind speed from 0.5 to 6 m s^{-1} with an interval of 0.5 m s^{-1}.

3.2. Physical Processes

Detailed 0–20 m upper ocean processes driving the inhomogeneous SST warming along the Kuroshio were examined using metocean buoy observations (Figure 3). The observations revealed two diurnal SST warming events: (a) the SST warming event 7 in the southern part (10–40 km) of wind bifurcation where the wind is moderate and (b) the SST warming event 8 around and in the northern part of wind bifurcation (130–180 km) where the wind was low (Figures 2b and 2c). The solar insolation (magenta line in Figure 3a) dominated near surface layer heating in the daytime (Figure 3b), forming the DWL that spawned the daily SST warming. The DWL event on 7 September was first interpreted. The buoy-measured apparent wind speed during the DWL event had a mean value of 3.5 m s^{-1} (black curve in Figure 3a). As enclosed by the 30°C isotherm, the solar heat was trapped in the upper ~5 m. Wind stress accelerated a jet in this layer. A southwestward flowing jet formed at ~12:00 (vertical dashed line), roughly identical to the wind-blowing direction (Figure 3e), was collocated with DWL. The jet, having a speed of ~0.1 m s^{-1}, has been referred to as the "diurnal jet" (Hughes et al., 2020; Price et al., 1986; Sutherland et al., 2016; Wijesekera et al., 2020) in response to the momentum from the wind trapped in the DWL. Notably, the diurnal jet appeared as an inertial rotation in a clockwise (rightward) manner, from south-southwest to west-southwest. The jet then weakened and deepened to 8 m in early nighttime (18:00–21:00). The diurnal warming and jet respectively generated strong stratification (characterized by $4N^2$; Figure 3f and Text S1 in Supporting Information S1) and shear (characterized by shear squared S^2; Figure 3g and Text S1 in Supporting Information S1) in the DWL, which could stabilize and destabilize the water layer, respectively. The clear colocation of strong shear and stratification (Figures 3f and 3g) suggested their complex interactions.

To clarify further, we computed the reduced shear squared as S^2–$4N^2$ (Figure 3h), which has a positive value when $Ri = N^2/S^2 < 0.25$, that is, the indication of the possible occurrence of shear instability (Howard, 1961; Miles, 1961). When S^2–$4N^2$ is negative, $Ri > 0.25$, and shear instability is inhibited. Frequent occurrences of shear instability were evident in the DWL because the condition S^2–$4N^2 > 0$ was reached (Figure 3h). However, both positive and negative values were present. The probability density distribution of S^2–$4N^2$ within the DWL fluctuates at a central value of 0 (Figure 4a), an indicator of marginal instability (Chang, 2021; Smyth, 2020; Thorpe & Liu, 2009). A state of equilibrium was reached between the wind forcing and resultant turbulent mixing. The current shear provided by the wind stress continuously increases S^2–$4N^2$ and eventually yields shear instability when S^2–$4N^2 \geq 0$. The effect of the resultant turbulence smooths the velocity and density differences until S^2–$4N^2 < 0$, and the status returns to stability. The repeated cyclic process makes the value of S^2–$4N^2$

concentrate around 0 (Smyth et al., 2019). The heat from the insolation would likely be well-mixed in the DWL under the above processes. The instability could extend downward in the nighttime until 21:00 (Figure 3h).

By contrast, the DWL on 8 September was inhibited in the upper 2 m (Figure 3b) when the mean wind speed was 2.2 m s^{-1} (black curve in Figure 3a). The near-surface temperature is 30.6°C–30.8°C, 0.5°C higher than 7 September. In the daytime, the diurnal jet was absent (Figures 3c and 3d). The strong stratification due to the buoyancy flux dominated the DWL (Figure 3f), leading to a stable condition where S^2–$4N^2 < 0$ (Figure 3h). The absence of shear instability in the daytime during the low wind condition prevented the insolation heat from mixing into the subsurface and, thus, accumulated heat on the near surface. The wind forcing was insufficient to deepen the DWL such that the insolation heating near the surface spread downward until nocturnal convective cooling beginning around 16:00. Our observations well explain the inhomogeneous diurnal SST warming in response to the insolation and the topography-modified wind (Figure 2). The critical wind speed U_{cr} ~2–3 m s^{-1} can be an indicator to separate the above two DWL regimes. In addition, the wind-induced flow advection could play a role in the nighttime warming (see Text S4 in Supporting Information S1). In this study, we focused on daytime SST warming.

4. Discussion and Conclusion

The SST warming in response to the solar insolation was most remarkable from 09:00 to 15:00 (Figure 2b). Using the data points shown in Figure 2b, AHI SST averaged in 9:00–15:00 (T_{AHI}) was well correlated with CCMP apparent wind speed at 08:00 (U_a), as shown in the scatter plot (yellow dots in Figure 4b). They had a correlation coefficient of 0.77, and a relation of $T_{AHI} = 30.82–0.144U_a$ was obtained from the linear regression (blue dashed line). The correlation lowered to 0.2 if the true wind speed was instead used (plus signs). Our observations (blue stars) well agreed with the regression line. The Price-Weller-Pinkel (PWP) model (Price et al., 1986), based on the shear-induced mixing, well explained the relationship. The PWP model results using the buoy-measured background temperature profile and insolation and the given constant wind speed from 0.5 to 6 m s^{-1} showed a curve (red curve in Figure 4b) that approached the preceding regression line (blue dashed line). Noticeably, a considerable SST drop appeared at ~2 m s^{-1} in the PWP curve, indicating a critical condition of SST variations as a function of wind speed. The U_a–T_{AHI} distribution did not clearly show a similar trend, presumably due to the insufficient spatiotemporal resolution of CCMP wind. Still, a clue can be found. The value of T_{AHI} fluctuated around the regression line when $U_a > 2$ m s^{-1}. In contrast, the value of T_{AHI} was mostly smaller than that in the regression line when $U_a < 2$ m s^{-1}. Therefore, U_{cr} is likely to be around 2 m s^{-1}. Hughes et al. (2020) also found a similar critical wind speed. Our observations support the critical wind speed of ~2 m s^{-1} and further highlight its importance in leading to inhomogeneous SST warming, particularly in the coastal ocean, where the wind could be modified in space.

Ideally, the warmest SST should be located centered on the bifurcation points. However, the warming SST events 6–10 revealed that the warmest SST was at the north of their bifurcation points (Figure 2b). Event 7 was further examined because it was the clearest case, as shown in Figure 1a, and the current measurement was available. A warm water region with SST >32°C centered approximately at the cyan plus sign (Figure 1a), ~40 km north of the wind bifurcation point. This can be explained as the combined effect of the advection and the time needed for warming in response to insolation. The warmest water was not around the bifurcation point because the water there was advected from its upstream where the wind speed was larger. The most effective warming occurred around the bifurcation point. The warmest water would translate ~16 km downstream from the bifurcation point, assuming the wind and insolation remain unchanged and the advection speed of 1.5 m s^{-1} and the lagging time of 3 hr was given. The accurate location may be obtained via a complete heat budget estimate, but this is not feasible based on our present data.

In summary, the diurnal SST variations and their physical mechanisms along the Kuroshio main axis off Taiwan may be unique compared to the typical diurnal variation in the open ocean. Under the clear sky and easterly wind conditions, inhomogeneous diurnal SST warming along the Kuroshio occurs due to the combined effects of orographically affected wind and the northeastward flowing current. The synoptic easterly wind bifurcates as it encounters Taiwan's coast, forming the southward-blowing and the northward-blowing winds above the Kuroshio. Therefore, a pair of regions having weakened and enhanced apparent wind speed relative to the Kuroshio was formed. The former (<2 m s^{-1}) has an enhanced SST warming because the solar heat is only trapped in the upper 2 m. The latter has a gentle SST warming due to the turbulence-induced downward heat transfer via

shear instability. The above processes are subject to Kuroshio's main axis position, which could be modulated by the mesoscale eddy (Chang et al., 2018). We further examined the SST in 2021 in the Kuroshio off the eastern coast of Taiwan in response to the synoptic wind (see Text S5 in Supporting Information S1 for details). SST enhancement on the windward side is 66 days in 2021, primarily in May and September, suggesting a probability of occurrence of 18% in a year.

Data Availability Statement

Data used to produce the figures can be obtained from https://doi.org/10.5281/zenodo.7107142. The Himawari 8/9 satellite SST data is available from the JAXA's P-Tree system (https://www.eorc.jaxa.jp/ptree/; required registration). CMEMS Satellite geostrophic velocity were obtained from https://doi.org/10.48670/moi-00148. The CCMP Version-2.0 wind analyses are produced by RSS (http://www.remss.com/support/data-shortcut/). SST products derived from Suomi NPP VIIRS can be downloaded from https://oceandata.sci.gsfc.nasa.gov/directdataaccess/Level-2/SNPP-VIIRS.

Acknowledgments
The metocean measurements and the analysis works were supported by Taiwan's National Science and Technology Council (NSTC) under Grants 110-2611-M-002-009 and 110-2611-M-002-026. The authors thank the crew and officers of the *R/V New Ocean Researcher 2* (NOR2) for the ship's operation. The technical supports from the Marine Instrument Center of NTU are essential to the success of the fieldwork. Experiments were greatly aided by the hard work of Shian-Chih Shie, Shih-Hong Wang, Bee Wang, Chen-Chen Ho, Dai-Jun Yu, and Yu-Ming Huang. Dr. Sally Warner, OSU, maintains the MATLAB code of the PWP model used in this study. We thank two anonymous reviewers whose comments significantly improved the original manuscript.

References

Alpers, W., Chen, J.-P., Lin, I.-I., & Lien, C.-C. (2007). Atmospheric fronts along the East Coast of Taiwan studied by ERS synthetic aperture radar images. *Journal of the Atmospheric Sciences*, *64*(3), 922–937. https://doi.org/10.1175/jas3863.1

Atlas, R., Hoffman, R. N., Ardizzone, J., Leidner, S. M., Jusem, J. C., Smith, D. K., & Gombos, D. (2011). A cross-calibrated, multiplatform ocean surface wind velocity product for meteorological and oceanographic applications. *Bulletin of the American Meteorological Society*, *92*(2), 157–174. https://doi.org/10.1175/2010bams2946.1

Basterretxea, G., Barton, E. D., Tett, P., Sangra, P., Navarro-Perez, E., & Aristegui, J. (2002). Eddy and deep chlorophyll maximum response to wind-shear in the lee of Gran Canaria. *Deep-Sea Research, Part A: Oceanographic Research Papers I*, *49*(6), 1087–1101. https://doi.org/10.1016/s0967-0637(02)00009-2

Caldeira, R. M. A., & Marchesiello, P. (2002). Ocean response to wind sheltering in the Southern California bright. *Geophysical Research Letters*, *29*(13), 1635. https://doi.org/10.1029/2001gl014563

Chang, M.-H. (2021). Marginal instability within internal solitary waves. *Geophysical Research Letters*, *48*(9), e2021GL092616. https://doi.org/10.1029/2021gl092616

Chang, M.-H., Jan, S., Mensah, V., Andres, M., Rainville, L., Yang, Y. J., & Cheng, Y.-H. (2018). Zonal migration and transport variations of the Kuroshio east of Taiwan induced by eddy impingements. *Deep-Sea Research Part I Oceanographic Research Papers*, *131*, 1–15. https://doi.org/10.1016/j.dsr.2017.11.006

Chen, T. C., Yen, M. C., Hseih, J. C., & Arritt, R. W. (1999). Diurnal and seasonal variations of the rainfall measured by the automatic rainfall and meteorological telemetry system in Taiwan. *Bulletin of the American Meteorological Society*, *80*(11), 2299–2312. https://doi.org/10.1175/1520-0477(1999)080<2299:dasvot>2.0.co;2

D'Asaro, E., Lee, C., Rainville, L., Harcourt, R., & Thomas, L. (2011). Enhanced turbulence and energy dissipation at ocean fronts. *Science*, *332*(6027), 318–322. https://doi.org/10.1126/science.1201515

Emanuel, K. A., & Sobel, A. (2013). Response of tropical sea surface temperature, precipitation, and tropical cyclone-related variables to changes in global and local forcing. *Journal of Advances in Modeling Earth Systems*, *5*(2), 447–458. https://doi.org/10.1002/jame.20032

Fairall, C. W., Bradley, E. F., Hare, J. E., Grachev, A. A., & Edson, J. B. (2003). Bulk parameterization of air-sea fluxes: Updates and verification for the COARE algorithm. *Journal of Climate*, *16*(4), 571–591. https://doi.org/10.1175/1520-0442(2003)016<0571:bpoasf>2.0.co;2

Howard, L. N. (1961). Note on a paper by J. W. Miles. *Journal of Fluid Mechanics*, *10*(04), 509–512. https://doi.org/10.1017/s0022112061000317

Hughes, K. G., Moum, J. N., & Shroyer, E. L. (2020). Evolution of the velocity structure in the diurnal warm layer. *Journal of Physical Oceanography*, *50*(3), 615–631. https://doi.org/10.1175/jpo-d-19-0207.1

Hwang, W.-C., Lin, P.-H., & Yu, H. (2020). The development of the "Storm Tracker" and its applications for atmospheric high-resolution upper-air observations. *Atmospheric Measurement Techniques*, *13*(10), 5395–5406. https://doi.org/10.5194/amt-13-5395-2020

Kawai, Y., & Wada, A. (2007). Diurnal sea surface temperature variation and its impact on the atmosphere and ocean: A review. *Journal of Oceanography*, *63*(5), 721–744. https://doi.org/10.1007/s10872-007-0063-0

Masich, J., Kessler, W. S., Cronin, M. F., & Grissom, K. R. (2021). Diurnal cycles of near-surface currents across the tropical Pacific. *Journal of Geophysical Research: Oceans*, *126*(4), e2020JC016982. https://doi.org/10.1029/2020jc016982

Mears, C. A., Scott, J., Wentz, F. J., Ricciardulli, L., Leidner, S. M., Hoffman, R., & Atlas, R. (2019). A near-real-time version of the cross-calibrated multiplatform (CCMP) ocean surface wind velocity data set. *Journal of Geophysical Research: Oceans*, *124*(10), 6997–7010. https://doi.org/10.1029/2019jc015367

Miles, J. W. (1961). On the stability of heterogeneous shear flows. *Journal of Fluid Mechanics*, *10*(04), 496–508. https://doi.org/10.1017/s0022112061000305

Price, J. F., Weller, R. A., & Pinkel, R. (1986). Diurnal cycling: Observations and models of upper ocean response to diurnal heating, cooling, and wind mixing. *Journal of Geophysical Research*, *91*(C7), 8411–8427. https://doi.org/10.1029/jc091ic07p08411

Shcherbina, A. Y., D'Asaro, E. A., & Harcourt, R. R. (2019). Rain and sun create slippery layers in the Eastern Pacific fresh pool. *Oceanography*, *32*(2), 98–107. https://doi.org/10.5670/oceanog.2019.217

Smyth, W. (2020). Marginal instability and the efficiency of ocean mixing. *Journal of Physical Oceanography*, *50*(8), 2141–2150. https://doi.org/10.1175/jpo-d-20-0083.1

Smyth, W., Nash, J., & Moum, J. (2019). Self-organized criticality in geophysical turbulence. *Nature Scientific Reports*, *9*(1), 3747. https://doi.org/10.1038/s41598-019-39869-w

Sui, C.-H., Li, X., & Lau, K.-M. (1998). Selective absorption of solar radiation and upper ocean temperature in the equatorial western Pacific. *Journal of Geophysical Research*, *103*(C5), 10313–10321. https://doi.org/10.1029/98jc00453

Sutherland, G., Marié, L., Reverdin, G., Christensen, K. H., Broström, G., & Ward, B. (2016). Enhanced turbulence associated with the diurnal jet in the ocean surface boundary layer. *Journal of Physical Oceanography*, *46*(10), 3051–3067. https://doi.org/10.1175/jpo-d-15-0172.1

Thompson, E. J., Moum, J. N., Fairall, C. W., & Rutledge, S. A. (2019). Wind limits on rain layers and diurnal warm layers. *Journal of Geophysical Research: Oceans*, *124*(2), 897–924. https://doi.org/10.1029/2018jc014130

Thorpe, S., & Liu, Z. (2009). Marginal instability? *Journal of Physical Oceanography*, *39*(9), 2373–2381. https://doi.org/10.1175/2009jpo4153.1

Wijesekera, H. W., Wang, D. W., & Jarosz, E. (2020). Dynamics of the diurnal warm layer: Surface jet, high-frequency internal waves, and mixing. *Journal of Physical Oceanography*, *50*(7), 2053–2070. https://doi.org/10.1175/jpo-d-19-0285.1

Wu, C.-C., Lee, C.-Y., & Lin, I.-I. (2007). The effect of the ocean eddy on tropical cyclone intensity. *Journal of the Atmospheric Sciences*, *64*(10), 3562–3578. https://doi.org/10.1175/jas4051.1

Yu, C.-K., & Lin, C.-Y. (2008). Statistical location and timing of the convective lines off the mountainous coast of southeastern Taiwan from long-term radar observations. *Monthly Weather Review*, *136*(12), 5077–5094. https://doi.org/10.1175/2008mwr2555.1

Yu, C.-K., & Lin, C.-Y. (2017). Formation and maintenance of a long-lived Taiwan rainband during 1–3 March 2003. *Journal of the Atmospheric Sciences*, *74*(4), 1211–1232. https://doi.org/10.1175/jas-d-16-0280.1